Editors' Suggestion

Room-Temperature Skyrmions at Zero Field in Exchange-Biased Ultrathin Films

K. Gaurav Rana,[1] A. Finco,[2] F. Fabre,[2] S. Chouaieb,[2] A. Haykal,[2] L. D. Buda-Prejbeanu,[1] O. Fruchart,[1] S. Le Denmat,[3] P. David,[3] M. Belmeguenai,[4] T. Denneulin,[5] R. E. Dunin-Borkowski,[5] G. Gaudin,[1] V. Jacques,[2,*] and O. Boulle[1,†]

[1] *Université Grenoble Alpes, CNRS, CEA, Grenoble INP, Spintec, Grenoble, France*
[2] *Laboratoire Charles Coulomb, Université de Montpellier and CNRS, 34095 Montpellier, France*
[3] *Université Grenoble Alpes, CNRS, Institut Néel, 38000 Grenoble, France*
[4] *Université Sorbonne Paris Nord, LSPM, CNRS, UPR 3407, 93430 Villetaneuse, France*
[5] *Ernst Ruska-Centre for Microscopy and Spectroscopy with Electrons and Peter Grünberg Institute, Forschungszentrum Jülich, 52425 Jülich, Germany*

(Received 24 January 2020; accepted 30 March 2020; published 30 April 2020)

We demonstrate that magnetic skyrmions with a mean diameter around 60 nm can be stabilized at room temperature and zero external magnetic field in an exchange-biased Pt/Co/$Ni_{80}Fe_{20}$/$Ir_{20}Mn_{80}$ multilayer stack. This is achieved through an advanced optimization of the multilayer-stack composition in order to balance the different magnetic energies controlling the skyrmion size and stability. Magnetic imaging is performed both with magnetic force microscopy and scanning nitrogen-vacancy magnetometry, the latter providing unambiguous measurements at zero external magnetic field. In such samples, we show that exchange bias provides an immunity of the skyrmion spin texture to moderate external-magnetic-field perturbations, in the tens-of-millitesla range, which is an important feature for applications such as memory devices. These results establish exchange-biased multilayer stacks as a promising platform toward the effective realization of memory and logic devices based on magnetic skyrmions.

DOI: 10.1103/PhysRevApplied.13.044079

I. INTRODUCTION

Magnetic skyrmions are whirling spin textures, which hold great promise for the storage and processing of information at the nanoscale in future memory and logic devices. These topological spin textures were initially observed at low temperature and in the presence of large magnetic fields, both in bulk materials exhibiting broken inversion symmetry [1,2] and in epitaxial ultrathin films with interfacial Dzyaloshinskii-Moriya interactions [3,4]. After years of active research, magnetic skyrmions can nowadays be stabilized at room temperature in technologically relevant materials based on sputtered magnetic multilayer stacks lacking inversion symmetry [5–8]. Deterministic skyrmion nucleation and fast current-induced motion (>100 m/s) have also recently been demonstrated, owing to the efficient spin-orbit torques in such magnetic multilayer stacks [6,9–14]. These results have opened a path for memory and logic devices where skyrmions in tracks are used as information carriers. Their particlelike topologically stable spin texture, small size, and efficient current-induced manipulation could lead to spintronic devices that provide a unique combination of high-density data-storage capabilities, high-speed logic operations, and low energy consumption [15,16].

To realize such devices, small-sized skyrmions must be stabilized at ambient conditions without the need for an external magnetic field. This challenging task can be pursued by using confined geometries [7,17,18], metastable skyrmion textures induced by pinning effects [19,20], frustration of exchange interactions in ultrathin ferromagnets [21], or ferrimagnetic materials close to the magnetization compensation [22]. Another promising strategy consists in designing magnetic heterostructures in which interlayer exchange coupling acts as an effective *internal* magnetic field B_{int} [23–25]. Here, we demonstrate that magnetic skyrmions with a mean diameter of around 60 nm can be stabilized at room temperature and zero external magnetic field in an ultrathin ferromagnetic layer that is exchange biased by an antiferromagnetic film. Compared to previous studies using exchange-biased multilayer stacks [24], this result corresponds to a reduction of the skyrmion diameter by one order of magnitude. This is achieved through an advanced optimization of the multilayer-stack composition in order to balance the different magnetic energies controlling the skyrmion size and stability [26,27].

*vincent.jacques@umontpellier.fr
†olivier.boulle@cea.fr

II. SAMPLE PREPARATION

The studied exchange-biased sample consists of a Ta/Pt(3)/Co(0.3)/$Ni_{80}Fe_{20}(t_{Ni_{80}Fe_{20}})$/$Ir_{20}Mn_{80}(t_{Ir_{20}Mn_{80}})$/Pt(3) multilayer stack (units in nanometers) deposited by magnetron sputtering on a 100-mm-diameter Si substrate [Fig. 1(a)]. The Pt/Co interface yields perpendicular magnetic anisotropy combined with a sizable interfacial Dzyaloshinskii-Moriya interaction (DMI) [28,29], which is a key ingredient for stabilizing skyrmions. Furthermore, this interface provides large spin-orbit torques for efficient current-induced skyrmion motion [14]. The use of a $Ni_{80}Fe_{20}$ thin film offers (i) a large exchange bias at the interface with the $Ir_{20}Mn_{80}$ layer and (ii) a lower spontaneous magnetization compared to cobalt, so that small-sized skyrmions are expected owing to a reduced dipolar energy [26,27]. To induce exchange bias, the samples are annealed at 200 °C for 2 min under a large out-of-plane magnetic field, $B_z = 570$ mT. Element-resolved scanning-transmission-electron-microscopy (STEM) images of a cross section of the sample reveal sharp interfaces with negligible intermixing [Fig. 1(a)].

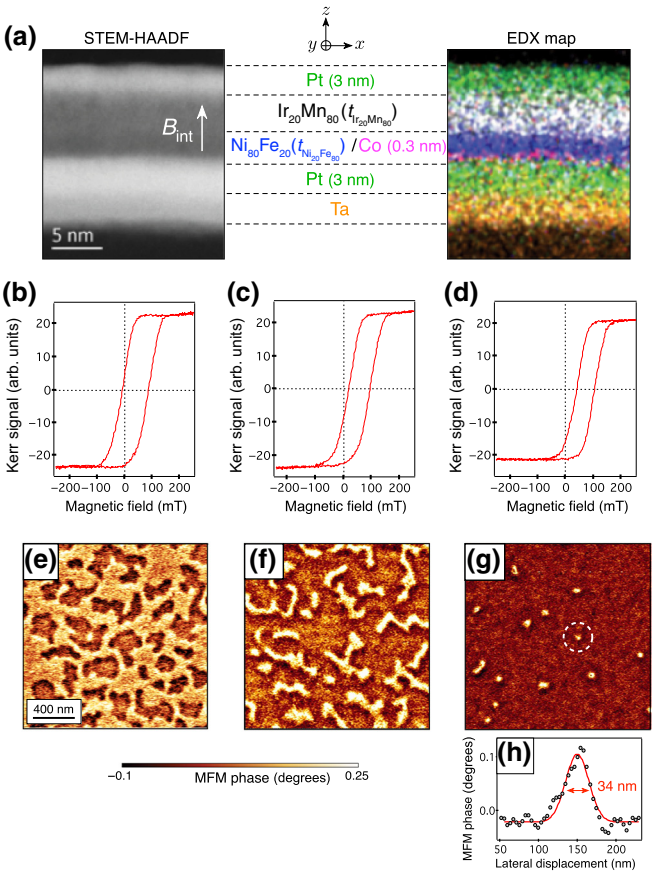

FIG. 1. (a) Central panel: the schematic structure of the exchange-biased multilayer stack. Left panel: a scanning-transmission-electron-microscopy image of a cross section of the sample obtained in a high-angle annular dark-field imaging (STEM-HAADF) mode. Right panel: energy-dispersive x-ray (EDX) elemental map. The white arrow indicates the direction of the internal exchange-bias field B_{int} across the $Ni_{80}Fe_{20}/Ir_{20}Mn_{80}$ interface. (b)–(d) Magneto-optical Kerr rotation recorded as a function of the magnetic field applied perpendicularly to the film plane for various $Ir_{20}Mn_{80}$ thicknesses: (b) $t_{Ir_{20}Mn_{80}} = 4$ nm, (c) $t_{Ir_{20}Mn_{80}} = 4.1$ nm, and (d) $t_{Ir_{20}Mn_{80}} = 4.2$ nm. For these experiments, the $Ni_{80}Fe_{20}$ thickness is $t_{Ni_{80}Fe_{20}} = 2.1$ nm. (e)–(g) Corresponding magnetic-force-microscopy (MFM) images recorded at zero external magnetic field. We note that no additional magnetic field is applied to the sample after the annealing procedure. (h) Line profile across the skyrmion marked with the white dashed circle in (g). The red solid line is a Gaussian fit, leading to a full width at half maximum (FWHM) $w_{MFM} = 34 \pm 3$ nm.

An important parameter controlling the skyrmion size and stability is the $Ni_{80}Fe_{20}$ film thickness, $t_{Ni_{80}Fe_{20}}$, since the main skyrmion energy terms, namely the magnetic anisotropy, the DMI, and the dipolar fields, are strongly dependent on the thickness of the ferromagnetic layer [7]. Similarly, the exchange bias and magnetic anisotropy are highly sensitive to the $Ir_{20}Mn_{80}$ film thickness $t_{Ir_{20}Mn_{80}}$ [24]. In order to find the optimal sample composition stabilizing zero-field skyrmions, gradients of $Ni_{80}Fe_{20}$ and $Ir_{20}Mn_{80}$ thicknesses are deposited along the x and y axes of the 100-mm wafer, respectively, using off-axis deposition. Systematic hysteresis-loop mapping is then carried out using the magneto-optical Kerr effect supplemented by magnetic force microscopy (MFM).

The optimal sample composition stabilizing zero-field skyrmions is achieved for a $Ni_{80}Fe_{20}$ thickness of around $t_{Ni_{80}Fe_{20}} = 2.1$ nm, close to the out-of-plane to in-plane transition of the magnetization, and an $Ir_{20}Mn_{80}$ thickness of around $t_{Ir_{20}Mn_{80}} = 4.2$ nm. Typical magnetic hysteresis loops recorded for different thicknesses of the $Ir_{20}Mn_{80}$ layer are shown in Figs. 1(b)–1(d). The observation of slanted hysteresis loops suggests the existence of multidomain states. In addition, these measurements indicate that the effective exchange-bias field B_{int}, characterized by the overall shift of the hysteresis loop, increases with the $Ir_{20}Mn_{80}$ film thickness, while the coercivity decreases. MFM images recorded at zero external magnetic field for different $Ir_{20}Mn_{80}$ thicknesses, i.e., for different exchange-bias fields B_{int}, are shown in Figs. 1(e)–1(g). For $t_{Ir_{20}Mn_{80}} = 4$ nm, the small exchange-bias field combined with a large coercivity of the ferromagnetic layer leads to a multidomain state, with a nearly equal density of up- and down-magnetized domains [Fig. 1(e)]. As the $Ir_{20}Mn_{80}$ thickness is slightly increased to $t_{Ir_{20}Mn_{80}} = 4.1$ nm, the down-magnetized domains start to shrink and few skyrmions can be observed [Fig. 1(f)]. A further increase in the $Ir_{20}Mn_{80}$ thickness ($t_{Ir_{20}Mn_{80}} = 4.2$ nm) leads to the stabilization of well-isolated skyrmions in the ferromagnetic layer [Fig. 1(g)]. The smallest skyrmions exhibit a FWHM down to approximately 35 nm in the MFM image [Fig. 1(h)].

In the following, we focus on the optimized Pt/Co(0.3)/$Ni_{80}Fe_{20}$(2.1)/$Ir_{20}Mn_{80}$(4.2) multilayer stack. Its effective saturation magnetization is measured by superconducting-

quantum-interference-device (SQUID) magnetometry, leading to $M_s = 720$ kA/m, while vibrating-sample magnetometry is used to infer the perpendicular magnetic anisotropy $K = 350$ kJ/m^3. The strength of the interfacial DMI is determined by monitoring the nonreciprocal propagation of spin waves with Brillouin-light-scattering (BLS) spectroscopy [28–30], yielding $D = -0.4$ mJ/m^2 (see the Appendix A). The negative value of the D parameter promotes the stabilization of Néel skyrmions with a left-handed chirality.

III. RESULTS AND DISCUSSION

A systematic study of the skyrmion size is realized through magnetic imaging with a scanning nitrogen-vacancy (N-V) magnetometer operated in photoluminescence- (PL) quenching mode at room temperature and zero external magnetic field [31]. Compared to MFM, the main advantage of this technique here is the absence of magnetic perturbations on the studied sample, thus providing unambiguous measurements at zero magnetic field. We employ a single N-V defect located at the apex of a nanopillar in a commercial diamond scanning-probe unit [32,33] (Qnami, Quantilever MX), which is integrated into an atomic force microscope and scanned in close proximity to the magnetic sample. At each point of the scan, a confocal optical microscope is used to record the PL signal of the N-V defect. Stray magnetic fields produced locally by spin textures in ferromagnets lead to an overall reduction of the PL signal [34–36]. Such a magnetic-field-induced PL quenching is exploited here to image magnetic skyrmions with a spatial resolution fixed by the distance between the N-V sensor and the ferromagnetic layer, $z_{\text{N-}V} \approx 65$ nm, as measured through an independent calibration procedure [37].

Figure 2(a) shows a typical PL-quenching image recorded at zero field above the optimized exchange-biased multilayer stack. Dark PL spots result from the stray field produced by isolated magnetic skyrmions. This observation confirms unambiguously the zero-field stability of skyrmions in the exchange-biased stack under ambient conditions. The FWHM w and the contrast $\mathcal{C}$ of the dark PL spots are inferred by fitting line profiles with a Gaussian function for a set of 51 isolated skyrmions [Fig. 2(b)]. The resulting statistics are shown in Figs. 2(c) and 2(d). Data fitting with a normal distribution leads to a mean value of the width $\bar{w} = 66 \pm 1$ nm, with a standard deviation $\sigma_w = 20 \pm 2$ nm [Fig. 2(c)]. For the PL-quenching contrast, which is linked to the stray-field amplitude, a mean value $\bar{\mathcal{C}} = 23 \pm 1\%$ is obtained with a standard deviation $\sigma_{\mathcal{C}} = 6 \pm 1\%$ [Fig. 2(d)]. In order to extract information on the actual skyrmion size from these experimental results, simulations of the PL-quenching image are performed for various skyrmion diameters. To this end, the skyrmion profile is simply modeled by a 360° Néel domain wall with

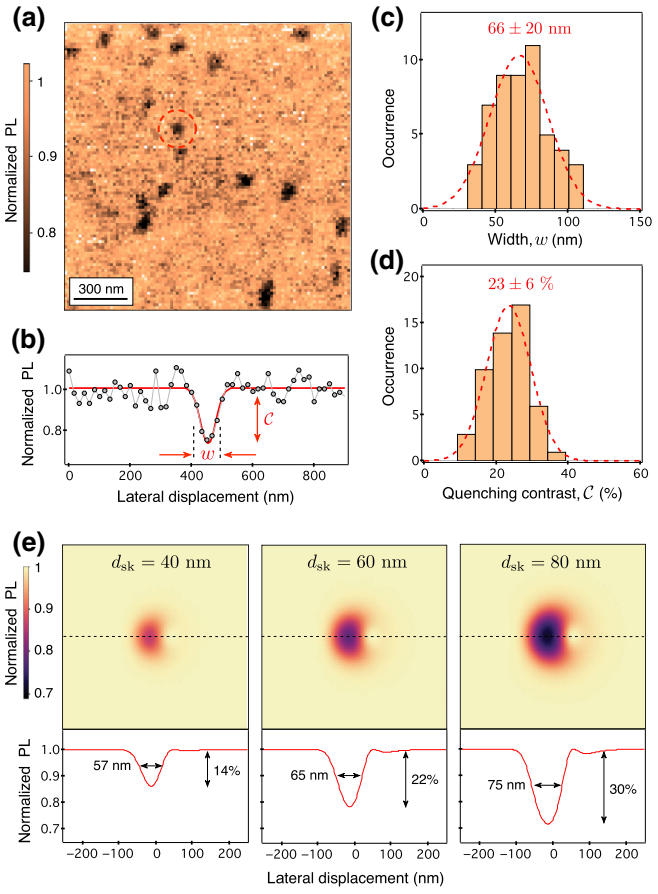

FIG. 2. (a) A N-V magnetometry image recorded in photoluminescence- (PL) quenching mode above the optimized exchange-biased multilayer stack at room temperature and zero external magnetic field. In these experiments, the distance between the N-V sensor and the ferromagnetic layer is approximately 65 nm. (b) Line profile across the skyrmion marked with the dashed circle in (a). The profile is taken along the fast-scan direction (horizontal) and the red solid line is a Gaussian fit, leading to a FWHM $w = 58 \pm 8$ nm and a PL quenching contrast $\mathcal{C} = 27 \pm 2\%$. (c),(d) Statistical distributions of (c) the width w and (d) the quenching contrast $\mathcal{C}$, inferred from measurements over a set of 51 isolated skyrmions. The dashed lines are data fitting with normal distributions. The values written on top of the histograms correspond to the mean value ± standard deviation of the distributions. (e) Simulations of the PL-quenching image resulting from the stray field produced by skyrmions with diameters $d_{\text{sk}} = 40$, 60, and 80 nm (from left to right). Line profiles taken across the skyrmions (black dashed lines) are displayed below the PL maps, indicating the width and the quenching contrast.

a left-handed chirality [38] and a characteristic domain-wall width $\sqrt{A/K_{\text{eff}}}$, where A is the exchange constant and $K_{\text{eff}} = K - \mu_0 M_s^2/2$ denotes the effective magnetic anisotropy. The exchange constant is fixed to $A = 6$ pJ/m, a value in line with measurements in permalloy ultrathin films [30]. The stray-field distribution is first calculated at the flying distance of the N-V sensor $z_{\text{N-}V} \approx 65$ nm

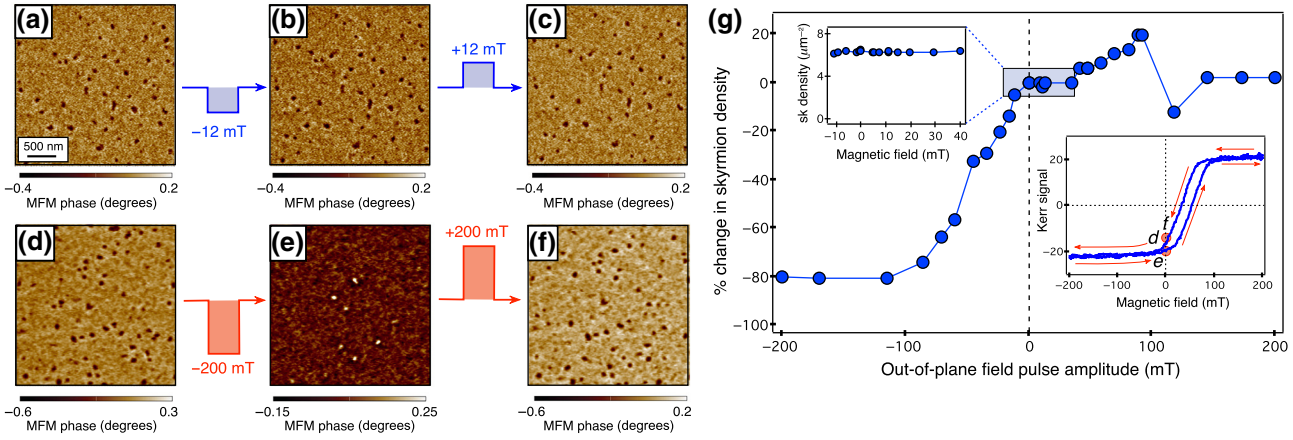

FIG. 3. (a)–(c) MFM images recorded at zero external magnetic field (a) before and (b),(c) after the application of an out-of-plane field pulse of a few seconds' duration of (b) −12 mT and (c) +12 mT. (d)–(f) The same experiment before (d) and after the application of a field pulse of (e) −200 mT and (f) +200 mT. The skyrmion size distributions extracted for these MFM images are shown in Appendixes A and B. (g) The percentage change in skyrmion density as a function of the magnetic-field-pulse amplitude. The top-left inset is an enlargement of the weak magnetic field amplitudes. The bottom-right inset is the hysteresis loop of the exchange-biased multilayer stack measured by recording the magneto-optical Kerr rotation as a function of the out-of-plane magnetic field. The letters (d)–(f) refer to the MFM images.

for different skyrmion diameters d_{sk}. The resulting PL-quenching images are then simulated by using the model of the magnetic-field-dependent photodynamics of the N-V defect described in Ref. [34]. Typical simulations of PL-quenching images are shown in Fig. 2(e). Note that the slightly asymmetric shape of the simulated images results from the orientation of the N-V–defect quantization axis, which is characterized by the polar coordinates ($\theta \sim 54°, \phi \sim 0°$) in the (x,y,z) reference frame. A fair agreement with experimental results is obtained for $d_{sk} =$ 60 nm, for both the measured mean values of the width and the PL-quenching contrast. We can thus conclude that skyrmions with diameters of around 60 nm are stabilized at zero field in our optimized exchange-biased sample, corresponding to a reduction of the skyrmion diameter by one order of magnitude compared to previous reports [24].

We note that smaller skyrmions, down to approximately 10-nm diameter, have recently been observed at zero field in ferrimagnetic thin films close to the magnetization compensation at room temperature. However, such skyrmions have been found as metastable states, with lifetimes limited to a few hours [22]. More generally, stable sub-100-nm skyrmions have been obtained at room temperature by using multiple repetitions of magnetic multilayers, in which the thermal stability is enhanced by the large sample thickness [15,16]. However, skyrmion stabilization always requires the application of external magnetic fields in such multilayer stacks. Our results therefore demonstrate the potential of exchange-biased multilayer stacks to stabilize small-sized skyrmions at zero external magnetic field in ultrathin magnetic films. In such samples, exchange bias may enhance the skyrmion stability, a behavior already pointed out for the magnetic moment of magnetic nanoparticles [39,40] or nanomagnets in magnetic-random-access-memory (MRAM) cells [41].

In order to characterize the impact of external-magnetic-field perturbations on the skyrmion stability, the magnetic landscape is systematically measured with MFM before and after the application of a pulse of a few seconds' duration of an out-of-plane magnetic field B_z. In these experiments, positive (negative) magnetic field pulses result in a dilatation (compression) of the skyrmion diameter, followed by relaxation at zero field. As an example, Figs. 3(a)–3(c) show MFM images recorded before [Fig. 3(a)] and after the application of a field pulse of either −12 mT [Fig. 3(b)] or +12 mT [Fig. 3(c)]. For such field amplitudes, the skyrmion pattern is not modified (see Appendix B). This observation indicates that the skyrmion size here is mainly governed by exchange bias rather than magnetic history and pinning effects [35]. The impact of larger fields is analyzed by measuring variations of the skyrmion density. As shown in Fig. 3(g), the skyrmion density is little affected by field pulses with amplitudes lying between −12 and +40 mT. For larger fields, different behavior is observed, depending on the pulse polarity. While the skyrmion density drops for negative field pulses below −20 mT, only small variations are observed for positive magnetic fields up to +200 mT. This observation can be understood by considering the hysteresis loop of the exchange-biased stack [see inset in Fig. 3(g)]. Negative magnetic fields tend to make skyrmions smaller and thus more unstable, possibly leading to their annihilation, which results in an overall reduction of the skyrmion density. Conversely, positive magnetic fields tend to enlarge

magnetic skyrmions, thus increasing their stability or leading to the nucleation of new skyrmions. An example of skyrmion patterns recorded at zero magnetic field before and after the application of a large magnetic field pulse of −200 mT are shown in Figs. 3(d) and 3(e). A significant decrease of the skyrmion density is observed together with a reversed MFM contrast, in qualitative agreement with the lower Kerr signal evidenced in the hysteresis loop [see inset in Fig. 3(g)]. However, most skyrmions of the initial state can be recovered at zero field after saturation by applying a large positive magnetic field pulse of +200 mT [Fig. 3(f)], which indicates a strong return-point memory of the sample [42]. The magnetic skyrmions are therefore imprinted in the material, most likely at pinning sites induced by thickness variations in the multilayer stack [35]. If an external magnetic field perturbs the domain structure, the information can be recovered after the application of a large magnetic field pulse.

IV. SUMMARY

In this paper, we show that magnetic skyrmions with diameters of around 60 nm can be stabilized at room temperature and zero magnetic field in an optimized exchange-biased Pt/Co/$Ni_{80}Fe_{20}$/$Ir_{20}Mn_{80}$ multilayer stack. In such samples, exchange bias provides an immunity of the skyrmion spin texture to moderate external-magnetic-field perturbations, in the tens-of-millitesla range, which is a significant feature for applications such as memory devices. These results establish exchange-biased multilayer stacks as a promising platform toward the effective realization of memory and logic devices based on the manipulation of topological spin textures.

ACKNOWLEDGMENTS

We thank A. Kovács for his help with the acquisition of the STEM data and W. Akhtar for N-*V*–magnetometry experiments. This research has received funding from the DARPA TEE program, the European Research Council (ERC) under the European Union's Horizon 2020 Research and Innovation program under Grant Agreements No. 639802 (IMAGINE) and No. 856538 (3D MAGiC), the French Agence Nationale de la Recherche through the projects TOPSKY (Grant No. ANR-17-CE24-0025) and SKYLOGIC (Grant No. ANR-17-CE24-0045). A.F. acknowledges financial support from the EU Horizon 2020 Research and Innovation program under the Marie Sklodowska-Curie Grant Agreement No. 846597 (DIMAF).

K.G.R. and A.F. contributed equally to this work.

APPENDIX A: BRILLOUIN-LIGHT-SCATTERING SPECTROSCOPY

The strength of the interfacial DMI in the optimized Pt/Co(0.3)/$Ni_{80}Fe_{20}$(2.1)/$Ir_{20}Mn_{80}$(4.2) multilayer stack is inferred through BLS spectroscopy [28–30]. The principle of this technique is as follows. The magnetization is saturated in the film plane by an external magnetic field and spin waves (SWs) propagating along the direction perpendicular to this field are probed by a laser with a well-defined wave vector k_{SW}. The DMI introduces a preferred handedness, leading to an energy difference between two SWs propagating with opposite wave vectors. This energy difference corresponds to a shift in frequency $\Delta f\ (k_{SW}) = f_s\,(k_{SW}) - f_{as}\,(k_{SW})$, where f_s and f_{as} are the Stokes and anti-Stokes frequencies, respectively. This frequency shift is directly related to the DMI by the following relation [29]:

$$\Delta f\,(k_{SW}) = 2\gamma k_{SW} D/\,(\pi M_s)\,,$$

where γ is the gyromagnetic ratio, M_s is the saturation magnetization, and D is the DMI effective constant.

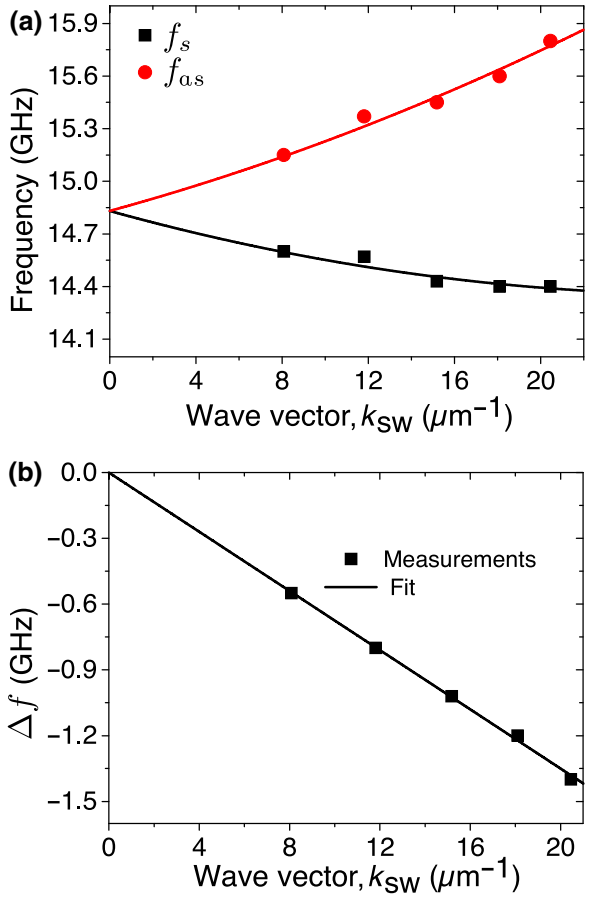

FIG. 4. (a) The frequency of the Stokes f_s (black) and anti-Stokes f_{as} (red) BLS lines as a function of k_{SW}. (b) $\Delta f = f_s - f_{as}$ as a function of k_{SW}.

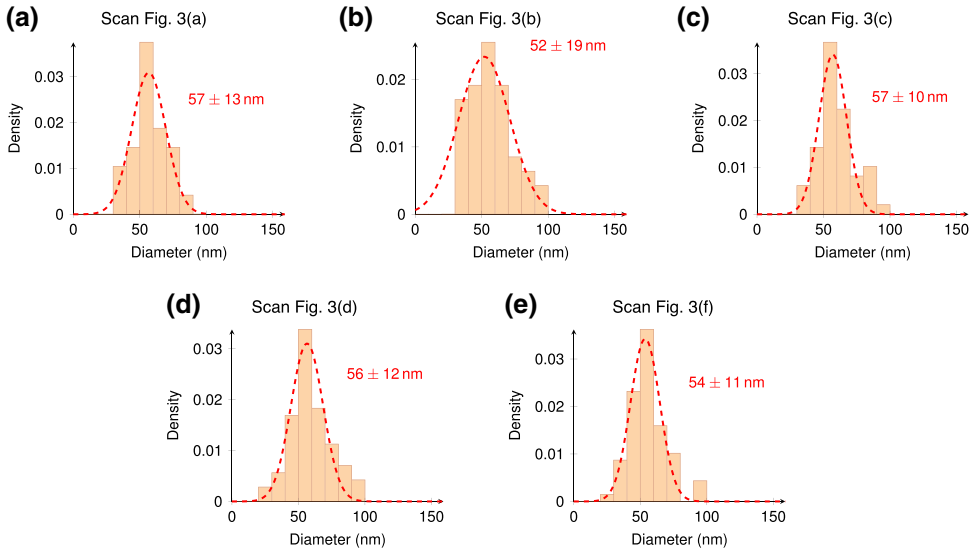

FIG. 5. Skyrmion size distributions extracted from the MFM images shown in Fig. 3.

Figure 4(a) shows the frequency of the Stokes and anti-Stokes peaks as a function of k_{SW}. The shift in frequency Δf scales linearly with k_{SW} [Fig. 4(a)], which allows us to extract $D = -0.4$ mJ/m^2, using $M_s = 720$ kA/m and $\gamma/(2\pi) = 31$ GHz/T extracted from ferromagnetic resonance experiments. In these BLS experiments, a negative value for D indicates a left-handed chirality, in line with previous works [7].

APPENDIX B: SKYRMION SIZE DISTRIBUTIONS EXTRACTED FROM MFM IMAGES

Figure 5 shows the skyrmion size distributions extracted from the MFM images recorded after the application of a pulse of a few seconds' duration of an out-of-plane magnetic field B_z [cf. Fig. 3]. These results show that the skyrmion size distribution is not modified after the application of magnetic field pulses.

[1] S. Mühlbauer, B. Binz, F. Jonietz, C. Pfleiderer, A. Rosch, A. Neubauer, R. Georgii, and P. Böni, Skyrmion lattice in a chiral magnet, Science **323**, 915 (2009).

[2] X. Z. Yu, Y. Onose, N. Kanazawa, J. H. Park, J. H. Han, Y. Matsui, N. Nagaosa, and Y. Tokura, Real-space observation of a two-dimensional skyrmion crystal, Nature (London) **465**, 901 (2010).

[3] S. Heinze, K. von Bergmann, M. Menzel, J. Brede, A. Kubetzka, R. Wiesendanger, G. Bihlmayer, and S. Blügel, Spontaneous atomic-scale magnetic skyrmion lattice in two dimensions, Nat. Phys. **7**, 713 (2011).

[4] N. Romming, C. Hanneken, M. Menzel, J. E. Bickel, B. Wolter, K. von Bergmann, A. Kubetzka, and R. Wiesendanger, Writing and deleting single magnetic skyrmions, Science **341**, 636 (2013).

[5] W. Jiang, P. Upadhyaya, W. Zhang, G. Yu, M. B. Jungfleisch, F. Y. Fradin, J. E. Pearson, Y. Tserkovnyak, K. L. Wang, O. Heinonen, S. G. E. te Velthuis, and A. Hoffmann, Blowing magnetic skyrmion bubbles, Science **349**, 283 (2015).

[6] S. Woo, K. Litzius, B. Krüger, M.-Y. Im, L. Caretta, K. Richter, M. Mann, A. Krone, R. M. Reeve, M. Weigand, P. Agrawal, I. Lemesh, M.-A. Mawass, P. Fischer, M. Kläui, and G. S. D. Beach, Observation of room-temperature magnetic skyrmions and their current-driven dynamics in ultrathin metallic ferromagnets, Nat. Mater. **15**, 501 (2016).

[7] O. Boulle *et al.*, Room-temperature chiral magnetic skyrmions in ultrathin magnetic nanostructures, Nat. Nanotech. **11**, 449 (2016).

[8] C. Moreau-Luchaire, C. Moutafis, N. Reyren, J. Sampaio, C. A. F. Vaz, N. Van Horne, K. Bouzehouane, K. Garcia, C. Deranlot, P. Warnicke, P. Wohlhüter, J.-M. George, M. Weigand, J. Raabe, V. Cros, and A. Fert, Additive interfacial chiral interaction in multilayers for stabilization of small individual skyrmions at room temperature, Nat. Nanotech. **11**, 444 (2016).

[9] A. Hrabec, J. Sampaio, M. Belmeguenai, I. Gross, R. Weil, S. M. Chérif, A. Stashkevich, V. Jacques, A. Thiaville, and S. Rohart, Current-induced skyrmion generation and dynamics in symmetric bilayers, Nat. Commun. **8**, 15765 (2017).

[10] F. Büttner, I. Lemesh, M. Schneider, B. Pfau, C. M. Günther, P. Hessing, J. Geilhufe, L. Caretta, D. Engel, B. Krüger, B. J. Viefhaus, S. Eisebitt, and G. S. D. Beach, Field-free deterministic ultrafast creation of magnetic skyrmions by spin-orbit torques, Nat. Nanotech. **12**, 1040 (2017).

[11] W. Legrand, D. Maccariello, N. Reyren, K. Garcia, C. Moutafis, C. Moreau-Luchaire, S. Collin, K. Bouzehouane, V. Cros, and A. Fert, Room-temperature current-induced generation and motion of sub-100 nm skyrmions, Nano Lett. **17**, 2703 (2017).

[12] S. Woo, K. M. Song, X. Zhang, M. Ezawa, Y. Zhou, X. Liu, M. Weigand, S. Finizio, J. Raabe, M.-C. Park, K.-Y. Lee, J. W. Choi, B.-C. Min, H. C. Koo, and J. Chang, Deterministic creation and deletion of a single

magnetic skyrmion observed by direct time-resolved x-ray microscopy, Nat. Electron. **1**, 288 (2018).

[13] S. Woo, K. Song, X. Zhang, Y. Zhou, M. Ezawa, X. Liu, S. Finizio, J. Raabe, N. J. Lee, S.-I. Kim, S.-Y. Park, Y. Kim, J.-Y. Kim, D. Lee, O. Lee, J. W. Choi, B.-C. Min, H. C. Koo, and J. Chang, Current-driven dynamics and inhibition of the skyrmion Hall effect of ferrimagnetic skyrmions in GdFeCo films, Nat. Commun. **9**, 959 (2018).

[14] R. Juge *et al.*, Current-Driven Skyrmion Dynamics and Drive-Dependent Skyrmion Hall Effect in an Ultrathin Film, Phys. Rev. Appl. **12**, 044007 (2019).

[15] A. Fert, N. Reyren, and V. Cros, Magnetic skyrmions: Advances in physics and potential applications, Nat. Rev. Mater. **2**, 17031 (2017).

[16] K. Everschor-Sitte, J. Masell, R. M. Reeve, and M. Klaui, Perspective: Magnetic skyrmions—overview of recent progress in an active research field, J. Appl. Phys. **124**, 240901 (2018).

[17] P. Ho, A. K. C. Tan, S. Goolaup, A. L. G. Oyarce, M. Raju, L. S. Huang, A. Soumyanarayanan, and C. Panagopoulos, Geometrically Tailored Skyrmions at Zero Magnetic Field in Multilayered Nanostructures, Phys. Rev. Appl. **11**, 024064 (2019).

[18] K. Zeissler, S. Finizio, K. Shahbazi, J. Massey, F. A. Ma'Mari, D. M. Bracher, A. Kleibert, M. C. Rosamond, E. H. Linfield, T. A. Moore, J. Raabe, G. Burnell, and C. H. Marrows, Discrete Hall resistivity contribution from Néel skyrmions in multilayer nanodiscs, Nat. Nano. **13**, 1161 (2018).

[19] N. K. Duong, M. Raju, A. P. Petrovic, R. Tomasello, G. Finocchio, and C. Panagopoulos, Stabilizing zero-field skyrmions in Ir/Fe/Co/Pt thin film multilayers by magnetic history control, Appl. Phys. Lett. **114**, 072401 (2019).

[20] K. Zeissler, S. Finizio, C. Barton, A. J. Huxtable, J. Massey, J. Raabe, A. V. Sadovnikov, S. A. Nikitov, R. Brearton, T. Hesjedal, G. van der Laan, M. C. Rosamond, E. H. Linfield, G. Burnell, and C. H. Marrows, Diameter-independent skyrmion Hall angle observed in chiral magnetic multilayers, Nat. Commun. **11**, 428 (2020).

[21] S. Meyer, M. Perini, S. von Malottki, A. Kubetzka, R. Wiesendanger, K. von Bergmann, and S. Heinze, Isolated zero field sub-10 nm skyrmions in ultrathin Co films, Nat. Commun. **10**, 3823 (2019).

[22] L. Caretta, M. Mann, F. Büttner, K. Ueda, B. Pfau, C. M. Günther, P. Hessing, A. Churikova, C. Klose, M. Schneider, D. Engel, C. Marcus, D. Bono, K. Bagschik, S. Eisebitt, and G. S. D. Beach, Fast current-driven domain walls and small skyrmions in a compensated ferrimagnet, Nat. Nanotech. **13**, 1154 (2018).

[23] G. Chen, A. Mascaraque, A. T. N'Diaye, and A. K. Schmid, Room temperature skyrmion ground state stabilized through interlayer exchange coupling, Appl. Phys. Lett. **106**, 242404 (2015).

[24] G. Yu, A. Jenkins, X. Ma, S. A. Razavi, C. He, G. Yin, Q. Shao, Q. He, H. Wu, W. Li, W. Jiang, X. Han, X. Li, A. C. Bleszynski Jayich, P. K. Amiri, and K. L. Wang, Room-temperature skyrmions in an antiferromagnet-based heterostructure, Nano Lett. **18**, 980 (2018).

[25] Y. Guang *et al.*, Creating zero-field skyrmions in exchange-biased multilayers through x-ray illumination, Nat. Commun. **11**, 949 (2020).

[26] F. Büttner, I. Lemesh, and G. S. D. Beach, Theory of isolated magnetic skyrmions: From fundamentals to room temperature applications, Sci. Rep. **8**, 4464 (2018).

[27] A Bernand-Mantel, L. Camosi, A. Wartelle, N. Rougemaille, M. Darques, and L. Ranno, The skyrmion-bubble transition in a ferromagnetic thin film, SciPost Phys. **4**, 27 (2018).

[28] K. Di, V. L. Zhang, H. S. Lim, S. C. Ng, M. H. Kuok, J. Yu, J. Yoon, X. Qiu, and H. Yang, Direct Observation of the Dzyaloshinskii-Moriya Interaction in a Pt/Co/Ni Film, Phys. Rev. Lett. **114**, 047201 (2015).

[29] M. Belmeguenai, J.-P. Adam, Y. Roussigné, S. Eimer, T. Devolder, J.-V. Kim, S. M. Cherif, A. Stashkevich, and A. Thiaville, Interfacial Dzyaloshinskii-Moriya interaction in perpendicularly magnetized Pt/Co/AlO_x ultrathin films measured by Brillouin light spectroscopy, Phys. Rev. B **91**, 180405 (2015).

[30] H. T. Nembach, J. M. Shaw, M. Weiler, E. Jué, and T. J. Silva, Linear relation between Heisenberg exchange and interfacial Dzyaloshinskii-Moriya interaction in metal films, Nat. Phys. **11**, 825 (2015).

[31] L. Rondin, J.-P. Tetienne, T. Hingant, J.-F. Roch, P. Maletinsky, and V. Jacques, Magnetometry with nitrogen-vacancy defects in diamond, Rep. Prog. Phys. **77**, 056503 (2014).

[32] P. Maletinsky, S. Hong, M. S. Grinolds, B. Hausmann, M. D. Lukin, R. L. Walsworth, M. Loncar, and A. Yacoby, A robust scanning diamond sensor for nanoscale imaging with single nitrogen-vacancy centres, Nat. Nanotech. **7**, 320 (2012).

[33] P. Appel, E. Neu, M. Ganzhorn, A. Barfuss, M. Batzer, M. Gratz, A. Tschope, and P. Maletinsky, Fabrication of all diamond scanning probes for nanoscale magnetometry, Rev. Sci. Instrum. **87**, 063703 (2016).

[34] J.-P. Tetienne, L. Rondin, P. Spinicelli, M. Chipaux, T. Debuisschert, J.-F. Roch, and V. Jacques, Magnetic-field-dependent photodynamics of single NV defects in diamond: An application to qualitative all-optical magnetic imaging, New J. Phys. **14**, 103033 (2012).

[35] I. Gross, W. Akhtar, A. Hrabec, J. Sampaio, L. J. Martínez, S. Chouaieb, B. J. Shields, P. Maletinsky, A. Thiaville, S. Rohart, and V. Jacques, Skyrmion morphology in ultrathin magnetic films, Phys. Rev. Mater. **2**, 024406 (2018).

[36] W. Akhtar, A. Hrabec, S. Chouaieb, A. Haykal, I. Gross, M. Belmeguenai, M. S. Gabor, B. Shields, P. Maletinsky, A. Thiaville, S. Rohart, and V. Jacques, Current-Induced Nucleation and Dynamics of Skyrmions in a Co-Based Heusler Alloy, Phys. Rev. Appl. **11**, 034066 (2019).

[37] T. Hingant, J.-P. Tetienne, L. J. Martínez, K. Garcia, D. Ravelosona, J.-F. Roch, and V. Jacques, Measuring the Magnetic Moment Density in Patterned Ultrathin Ferromagnets with Submicrometer Resolution, Phys. Rev. Appl. **4**, 014003 (2015).

[38] N. Romming, A. Kubetzka, C. Hanneken, K. von Bergmann, and R. Wiesendanger, Field-Dependent Size and Shape of Single Magnetic Skyrmions, Phys. Rev. Lett. **114**, 177203 (2015).

[39] V. Skumryev, S. Stoyanov, Y. Zhang, G. Hadjipanayis, D. Givord, and J. Nogues, Beating the superparamagnetic limit with exchange bias, Nature **423**, 850 (2003).

[40] R. F. L. Evans, R. Yanes, O. Mryasov, R. W. Chantrell, and O. Chubykalo-Fesenko, On beating the superparamagnetic limit with exchange bias, EPL **88**, 57004 (2009).

[41] I. L. Prejbeanu, M Kerekes, R. C. Sousa, H. Sibuet, O. Redon, B. Dieny, and J.-P. Nozières, Thermally assisted MRAM, J. Phys.: Condens. Matter **19**, 165218 (2007).

[42] M. S. Pierce, C. R. Buechler, L. B. Sorensen, J. J. Turner, S. D. Kevan, E. A. Jagla, J. M. Deutsch, T. Mai, O. Narayan, J. E. Davies, K. Liu, J. Hunter Dunn, K. M. Chesnel, J. B. Kortright, O. Hellwig, and E. E. Fullerton, Disorder-Induced Microscopic Magnetic Memory, Phys. Rev. Lett. **94**, 017202 (2005).